Evaluating the Utility of Mueller Matrix Imaging for Diffuse Material Classification

Meredith Kupinski and Lisa Li▲

Wyant College of Optical Sciences, The University of Arizona, 1630 E University Blvd, Tucson, AZ 85719
E-mail: meredith@optics.arizona.edu

Abstract. *Evaluating the utility of polarimetric imaging for material identification, as compared to conventional irradiance imaging, motivates this work. Images of diffuse objects captured with a wide field of view Mueller matrix polarimeter are used to demonstrate a classification and measurement optimization method. This imaging study is designed to test polarimetric utility in discriminating white fabric from white wood. The material color is constrained to be similar so that classification from only total radiance imaging is difficult, i.e., metamerism. A statistical divergence between two distributions of measured intensity is used to optimize the Polarization State Generator (PSG) and the Polarization State Analyzer (PSA) given two classes of Mueller matrices. The classification performance as a function of number of polarimetric measurements is computed. This work demonstrates that two polarimetric measurements of white fabric and white wood offer nearly perfect classification. The utility and design of partial Mueller imaging is supported by this optimization of PSG/PSA states and number of measurements.*
© *2020 Society for Imaging Science and Technology.*
[DOI: 10.2352/J.ImagingSci.Technol.2020.64.6.060409]

1. INTRODUCTION

The polarization state of light can be described using the real-valued Stokes parameters (also called a Stokes vector), a set of four numbers which represent the following properties of measured light

$$S = \begin{pmatrix} S_0 \\ S_1 \\ S_2 \\ S_3 \end{pmatrix} = \begin{pmatrix} P_{total} \\ P_{0°} - P_{90°} \\ P_{45°} - P_{135°} \\ P_R - P_L \end{pmatrix} = \begin{pmatrix} I \\ Q \\ U \\ V \end{pmatrix}. \qquad (1)$$

Here $P_{\phi°}$ is the radiance transmitted through a linear polarizer with a transmission-axis oriented in the $\phi°$ direction. For example, if $S_1 = 0$, the radiance measured through a horizontal linear polarizer and a vertical linear polarizer are equal. Thus, S_1 measures the excess of horizontal polarization over vertical polarization and is negative if $P_{90°} > P_{0°}$. The radiance transmitted through right- and left-circular polarizers are P_R and P_L, respectively. The first Stokes component is the total radiance leading to the constraint $S_0^2 \geq S_1^2 + S_2^2 + S_3^2$. The Stokes parameters are

frequently labeled I, Q, U, and V, particularly in remote sensing and astronomy [1].

Linear light-matter polarization effects are expressed as changes to the incident Stokes parameters after transmission or reflection

$$S_{out} = MS_{in}, \qquad (2)$$

where M is the Mueller matrix of the material. This 4×4 matrix is multiplied with the Stokes parameters of the incident state S_{in} to compute the exiting state S_{out}. Any changes in the wavelength, angle of incidence, or angle of observation will, in general, have a unique Mueller matrix. In imaging polarimetry, a Mueller matrix is reconstructed in a pixel-wise matter from a series of independent measurements. For each of these measurements the polarization state incident on the sample is given by the Polarization State Generator (PSG) and the polarization-dependent detection of the light reflected from the sample is given by the Polarization State Analyzer (PSA) [1]. To reconstruct the Mueller matrix, intensity measurements at unique PSG/PSA pairs form a system of linear equations,

$$\mathbf{p} = W^{\dagger} \mathbf{m}. \qquad (3)$$

Here $\mathbf{p}$ is a vector of intensity measurements, the 16 elements of the Mueller matrix are lexicographically ordered into a 16×1 vector $\mathbf{m}$, and the rows of $W^{\dagger}$ are constrained to satisfy fully polarized PSG/PSA states [2]. If W is a $16 \times K$ matrix where K is the number of intensity measurements made, then each row of $W^{\dagger}$ can be written as a Kronecker product between the kth PSG/PSA state as in

$$W^{\dagger} = \begin{pmatrix} \mathbf{a}_1 \otimes \mathbf{g}_1 \\ \mathbf{a}_2 \otimes \mathbf{g}_2 \\ \dots \\ \mathbf{a}_K \otimes \mathbf{g}_K \end{pmatrix}. \qquad (4)$$

Here $\mathbf{a}_l$ is a 4×1 vector of Stokes parameters describing the kth PSA, $\mathbf{g}_k$ is a 4×1 vector of Stokes parameters for the kth PSG. To form a full-rank system $K \geq 16$ [3]. The optimal choice of PSG/PSA states for Mueller matrix reconstruction was rigorously solved several decades ago [4]. However, researchers recognize that not all 16 Mueller matrix elements are necessary for many applications. Use of terms like "adaptive polarimetry" [5] and "partial polarimetry" [6, 7] appear in the literature and have been adopted in limited applications. A method to access the

information content of polarimetric measurements and inform the design of partial polarimetric systems for broad applications is still needed. This article reports analysis of polarimetric measurement utility to evaluate adaptive/partial polarimetry for diffuse material identification. Measurement utility relates an individual measurement to the performance of a scientific task as an empirical method for exploring a samples relevant optical properties [8, 9].

Polarimetry has been recognized as a tool for target discrimination for several decades [10]. Early results show clear demarcations between conducting metals and poorly conducting dielectrics [11]. Particle scattering in the Earth's atmosphere is the most notable application for which mathematical models of polarized light scattering and depolarization have been developed [12, 13]. In remote sensing, classification of ground targets from radar polarimetry combined with statistical decision-making techniques are well established [14]. Material classification for visible and near visible Mueller matrix imaging has been tested with a small field of view bench top imaging systems with an emphasis on post-processing algorithms and polarized light scattering models [15–18]. As the diffuse reflectance of a material increases, the degree of polarization of the scattered light decreases; this is known as the Umov Effect [19]. Materials with rough surfaces and high albedo like Spectralon and Teflon have been characterized in past work to have a small polarizing effect on scattered light [20]. This work demonstrates the optimization of polarimetric imaging to resolve metamerism in similarly high albedo dielectric materials which are diffusely scattering. The novel contributions of this article are: (1) demonstration of polarimetric imaging to resolve metamerism in diffusely scattering, dielectric materials, (2) a capture system optimization which yields nearly perfect classification from two polarimetric measurements, and (3) these two optimal measurements are non-linear polarization states and therefore not achievable by a commercially available linear Stokes cameras.

The rest of this article is organized as follows. Imaging hardware, acquisition, and the object ensembles are described in the Polarimetric Imaging System section. A detailed description of the J-optimal Channelized Quadratic Observer (J-CQO) used to optimize the PSG/PSA measurements is given in the Mathematical Methods section. Classification results are reported as area under the receiver operating characteristic (ROC) curve, otherwise known as the *AUC*, in the Classification Results section. Final observations, a summary of methods, and contributions are given in the Conclusions section.

2. POLARIMETRIC IMAGING SYSTEM

The RGB950 Mueller Matrix Imaging Polarimeter operates at 451, 524, 662, and 947 nm [21]. Figure 1 is a photograph of the instrument. The PSG is an LED array source followed by a diffuser, a fixed linear polarizer, a rotating 4" diameter multiplate achromatic retarder, and a similar-sized circular aperture. The retarder has a nominal retardance of one-third wave for the four operational wavelengths in the LED light
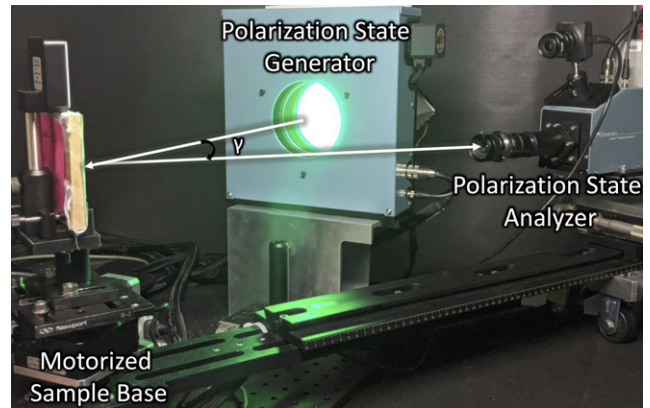

Figure 1. Photo of the RGB950 Mueller matrix imaging polarimeter. Note the illuminated circular aperture of the PSG. To the left of the PSG is the sample stage and the PSA is to the right. The sample normal bisects the scatter angle γ; this geometry images specular reflections.

box source. The PSA is a camera lens followed by a 1" diameter quartz retarder, 1" diameter linear polarizer, and an 8-bit detector. This unique instrument can produce videos of life-sized objects in a controlled environment where angle of incidence, angle of scatter, and sample orientation are precisely automated. The measurement studio is enclosed in a lightfast tent under which all reflecting surfaces and LED indicator lights are blocked.

Samples sit atop an automated base which consists of a rotation motor under a mounting base plate. The PSG hardware is fixed to an optical breadboard shared with the sample base to ensure optical and mechanical axis alignment. The breadboard itself is fixed to the optical table. The PSA hardware is attached to an XYZ translation stage which sits on an optical rail whose mechanical axis is aligned with the center of the sample base. The base is positioned at the point where the PSG/PSA hardwares' optical axes cross. The height of the PSA and the distance of the PSA to the sample stage is adjustable to account for a variety of object shapes and sizes. A ThorLabs camera is fixed to the PSA to capture RGB images of the samples. The ThorLabs camera's optical axis is parallel to the optical axis of the PSA in the sagittal plane.

The samples are positioned at the intersection of the axes for the source arm and camera arm. The sample normal bisects the scatter angle, labeled γ in Fig. 1. This geometry images specular reflections.

2.1 *Object Ensemble*

The object ensemble comprises materials which exhibit metamerism in RGB imaging to deliberately create a difficult material identification task for RGB images. The materials are reported in Table I and Figure 2 is a photograph of the samples. Color, texture, tone, and finish were considered when selecting materials. All materials selected are white in color to ensure a high albedo across the red, green, and blue color channels of the measurement instrument. Albedo is the diffuse reflectance of a material and has a inverse relationship with the degree of polarization, which is known as the Umov Effect [19].
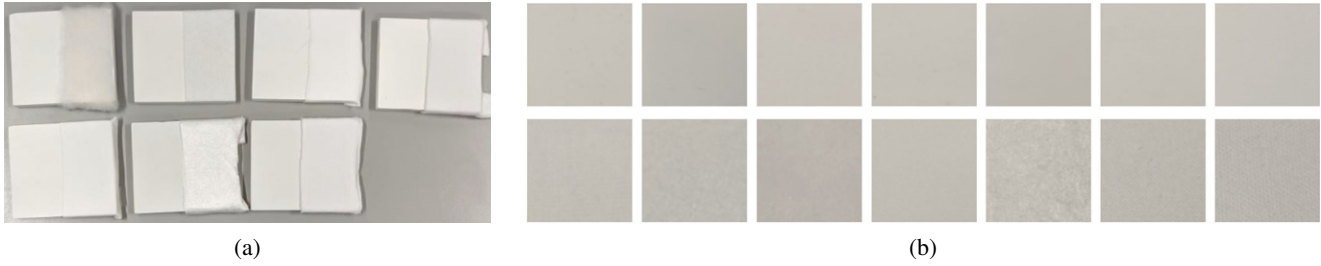
Figure 2. (a) RGB image of a sample set: seven objects consisting of white spray painted wood next to white fabric. (b) Small regions of the samples' RGB image removed from context. Top row is spray painted wood and bottom row is fabrics. These seven unique paints and seven unique fabrics are reported in Table I. The material color is similar so that classification from RGB imaging is difficult.

Table I. Fourteen objects: 7 painted wood and 7 fabric samples.

7 Paints	7 Fabrics
Ace Premium	Wool
Ace Rust-Oleum	Felt
Colorshot	Polyester
Krylon ColorMax	Cotton
Liquitex	97% Cotton /3% Spandex
Rust-Oleum	Silk
Rust-Oleum 2X	60% Cotton / 40% Polyester

All spray paints used in this study have a matte finish. Each spray paint is applied to a light wood panel in two even coats. Two coats of each paint were applied at a minimum to a wooden panel. Care is taken to keep the layers as thin as possible to avoid smoothing out the rough feature sizes in the wood panels. No sanding or priming treatment is used on the wooden panels before applying spray paint, and no additional finishing coats are applied to maintain a non-glossy finish. The seven white fabrics represent different sheens, material blends/types, and textures as described in Table I. All fabric samples are bleached to further match their color. Fabrics are ironed to ensure the samples are as flat as the painted wood.

3. MATHEMATICAL METHODS

3.1 *Partial Polarimetry*

To evaluate partial polarimetry L measurements are simulated from a measured Mueller matrix as in

$$i = T^\dagger m. \qquad (5)$$

Here T is a $16 \times L$ matrix where the columns are related to PSG/PSA states as in Eq. (4). Note that K is the number of measurements made to reconstruct the Mueller matrix and $L < K$; see Eq. (3).

The number of PSG/PSA parameters producing a single measurement can be reduced from eight (i.e., four elements of each Stokes vector a and g) to four (i.e., two coordinates on the surface of the Poincaré sphere for a and two for g). The surface of the Poincaré sphere represents all possible fully polarized states. A Stokes vector can be transformed to

coordinates on the Poincaré sphere by

$$\mathbf{a} = \begin{pmatrix} I_a \\ \rho_a \cos(2\psi_a)\cos(2\chi_a) \\ \rho_a \sin(2\psi_a)\cos(2\chi_a) \\ \rho_a \sin(2\chi_a) \end{pmatrix}, \qquad (6)$$

where I_a is the total radiance, ρ_a is the Degree of Polarization, ψ_a is the longitude, and χ_a is the latitude for the PSA [1]. Identical coordinates are defined for the PSG Stokes vector g denoted by the subscript. I_a and I_g are set to unity since any increase in total radiance would always increase the merit function for an otherwise fixed PSG/PSA. The Poincaré coordinates yield points on or within a sphere of unit radius: $0 \le \rho \le 1$, $-\pi/2 \le \psi \le \pi/2$, and $-\pi/4 \le \chi \le \pi/4$. Setting $\rho_a = \rho_g = 1$ constrains PSG/PSA solutions to be fully polarized states which are on the surface of the Poincaré sphere. States are partially polarized for $\rho < 1$. A partially polarized state is an incoherent sum of a fully polarized and an unpolarized state. Any addition of unpolarized light to a polarimetric measurement system is not desirable for reconstruction or classification tasks [22]. Therefore, the four variables subject to optimization for a single row of the matrix T are the longitude and latitude of the PSA and the longitude and latitude of the PSG, denoted $\boldsymbol{\theta} = [\psi_a, \chi_a, \psi_g, \chi_g]$.

3.2 *PSG/PSA Optimization*

The J-optimal Channelized Quadratic Observer (J-CQO) is used to optimize the PSG/PSA states given empirical distributions of Mueller matrix measurements from two classes [2]. The J-CQO optimizes Jeffrey's divergence (J) between two normal likelihoods: $pr(i|1)$ and $pr(i|2)$, where these are conditional probability density functions (PDF) of the intensity measurements i for each class (e.g., fabric or wood). The non-Gaussian distribution on the Mueller matrix is denoted: $pr_n(m)$. The first- and second-order moments are a 16×1 vector and a 16×16 matrix, denoted: $\overline{m}_n$ and K_n for each class $n = 1, 2$. Assume the intensity measurements are normally distributed where the mean of the nth class is an $L \times 1$ vector $\bar{i}_n = T^\dagger \overline{m}_n$ and the $L \times L$ covariance matrix is $C_n = T^t K_n T$. The dependence between the moments of the intensity measurements and the PSG/PSA could be made

explicit by denoting $\bar{i}_n(T)$ and $C_n(T)$. This dependence is dropped for brevity.

The scalar value of J between the L-dimensional normal PDFs $pr(i|1)$ and $pr(i|2)$ is

$$2J(T) = -2L + \mathrm{tr}\left[C_2^{-1} C_1\right]$$
$$+ \Delta\bar{i}^t C_2^{-1} \Delta\bar{i} + \mathrm{tr}\left[C_1^{-1} C_2\right] + \Delta\bar{i}^t C_1^{-1} \Delta\bar{i}, \quad (7)$$

where $\Delta\bar{i} = \bar{i}_1 - \bar{i}_2 = T^t(\overline{m}_1 - \overline{m}_2)$.

A closed-form gradient of Eq. (7) with respect to the matrix T and the PSG/PSA parameters θ can be found in [2]. This closed-formed gradient is the primary reason that the scalar value of J between two Gaussian distributions is an incredibly useful merit function. The Bhattacharyya distance has also been used to optimize a single PSG/PSA measurement without a closed-form gradient [5]. The mathematical and empirical relationship between J and AUC is described in [23].

3.3 Classification Task Performance

Objective assessment of image quality [24] quantifies the ability of an observer to use image data for performing a scientific task of interest, e.g., detection, classification, or estimation. Mathematical observers for detection or classification tasks operate on image data, or a post-processed version of the image data, to form a scalar-valued decision variable. ROC analysis provides the most comprehensive description of detection task performance, because it estimates and reports all of the combinations of sensitivity and specificity [25]. The area under the ROC curve, otherwise known as the AUC, is the gold standard figure of merit to quantify detection (i.e., binary classification) performance [24]. AUC is superior to other figures of merit for detection tasks that do not incorporate sensitivity and specificity [26]. The AUC ranges from 1.0 (i.e., classifier never makes a mistake) to 0.5 (i.e., classifier is guessing a decision). Another advantage of AUC is the operational definition as the percent correct on a two-alternative forced-choice test [25].

The Bayesian ideal observer maximizes the AUC as well as other task-based figures of merit using the log of the ratio of the likelihoods as a test statistic [27].

$$\Lambda(i) = \ln\left[pr(i|1)\right] - \ln\left[pr(i|2)\right]. \quad (8)$$

This expression simplifies for normal likelihoods to

$$\Lambda(i) = \left(i - \bar{i}_2\right)^t C_2^{-1}\left(i - \bar{i}_2\right) - \left(i - \bar{i}_1\right)^t C_1^{-1}\left(i - \bar{i}_1\right), \quad (9)$$

where terms that do not depend on i have been dropped.

A testing set and training set are created from the 7 fabric and 7 wood samples listed in Table I. The training set is used to compute a solution for the PSG/PSA states which maximize Eq. (7). The training set is also used to estimate the mean and covariance terms on the RHS of Eq. (9). Each Mueller matrix measurement in the testing set is used on the LHS of Eq. (9) to compute a test statistic and

Table II. Estimates of AUC from an **unpolarized** PSG/PSA (i.e., conventional irradiance imaging) at varying wavelengths λ and scattering angles γ. Mean and standard deviation are reported from five perturbations of the testing and training sets.

γ/λ	451 nm	524 nm	662 nm
20°	0.59 ± 0.05	0.55 ± 0.04	0.62 ± 0.09
30°	0.59 ± 0.09	0.57 ± 0.03	0.62 ± 0.03
40°	0.66 ± 0.09	0.62 ± 0.06	0.65 ± 0.06
50°	0.73 ± 0.07	0.65 ± 0.08	0.73 ± 0.03
60°	0.78 ± 0.06	0.68 ± 0.10	0.78 ± 0.03
70°	0.78 ± 0.09	0.69 ± 0.08	0.82 ± 0.05
80°	0.79 ± 0.13	0.70 ± 0.14	0.84 ± 0.09
90°	0.72 ± 0.08	0.67 ± 0.15	0.79 ± 0.13
100°	0.66 ± 0.09	0.66 ± 0.08	0.70 ± 0.08
110°	0.61 ± 0.02	0.59 ± 0.05	0.62 ± 0.09
120°	0.68 ± 0.08	0.61 ± 0.05	0.58 ± 0.04
130°	0.70 ± 0.19	0.65 ± 0.16	0.65 ± 0.09

Table III. Estimates of AUC from **randomly selected** PSG/PSA states. AUC is tabulated at varying scattering angles: γ and number of measurements: L. All results are for λ = 524 nm. The AUC is close to 1.0 at a majority of scattering angles for two measurements or greater. Mean and standard deviation are reported from five perturbations of the testing and training sets.

γ/L	1	2	3	4
20°	0.67 ± 0.06	0.82 ± 0.18	0.97 ± 0.03	0.95 ± 0.04
30°	0.68 ± 0.15	0.83 ± 0.17	0.92 ± 0.09	0.97 ± 0.02
40°	0.69 ± 0.15	0.93 ± 0.11	0.92 ± 0.07	0.99 ± 0.01
50°	0.68 ± 0.08	0.86 ± 0.17	0.96 ± 0.04	0.99 ± 0.01
60°	0.67 ± 0.14	0.92 ± 0.08	0.99 ± 0.01	0.99 ± 0.01
70°	0.66 ± 0.10	0.97 ± 0.02	0.99 ± 0.01	1.00 ± 0.00
80°	0.79 ± 0.15	0.94 ± 0.08	1.00 ± 0.01	1.00 ± 0.00
90°	0.74 ± 0.19	0.96 ± 0.08	1.00 ± 0.00	0.97 ± 0.05
100°	0.81 ± 0.17	0.98 ± 0.03	1.00 ± 0.00	1.00 ± 0.00
110°	0.79 ± 0.16	0.98 ± 0.05	1.00 ± 0.00	1.00 ± 0.00
120°	0.86 ± 0.17	0.91 ± 0.15	1.00 ± 0.00	1.00 ± 0.00
130°	0.89 ± 0.19	1.00 ± 0.00	0.99 ± 0.01	1.00 ± 0.00

estimate the AUC. Three images are selected for the training set and the remaining four images are the testing set. Five random selections without replacement are made to create independent combinations of the testing and training sets. From these five estimates of AUC the mean and standard deviation are reported in Tables II–IV.

4. CLASSIFICATION RESULTS

As a benchmark, the AUC is computed for a non-polarimetric imaging system. An unpolarized measurement is calculated from Eq. (5) using the unpolarized Stokes vector [1, 0, 0, 0] for both the PSA and the PSG. This
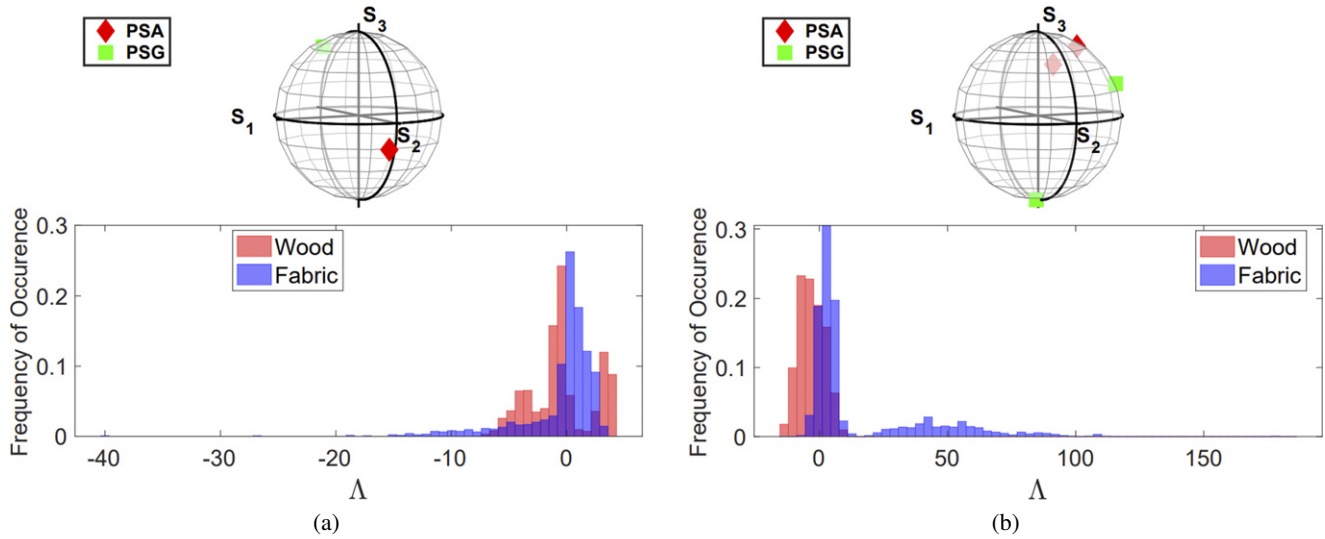
Figure 3. Poincaré sphere plot of **randomly selected** PSG/PSA states and histogram of test statistic: Λ (see Eq. (9)) for one instance of the five perturbations of testing and training images. In (a) single measurement ($L = 1$) and (b) two measurements ($L = 2$) from a single wavelength $\lambda = 524$ nm and single scattering angle $\gamma = 20°$ image. From Table III $\overline{AUC} = 0.67$ for $L = 1$ and $\overline{AUC} = 0.82$ for $L = 2$.

Figure 4. Poincaré sphere plot of **J-CQO optimized** PSG/PSA states and histogram of test statistic: Λ (see Eq. (9)) for one instance of the five perturbations of testing and training images. In (a) single measurement ($L = 1$) and (b) two measurements ($L = 2$) from a single wavelength $\lambda = 524$ nm and single scattering angle $\gamma = 20°$ image. From Table IV, $\overline{AUC} 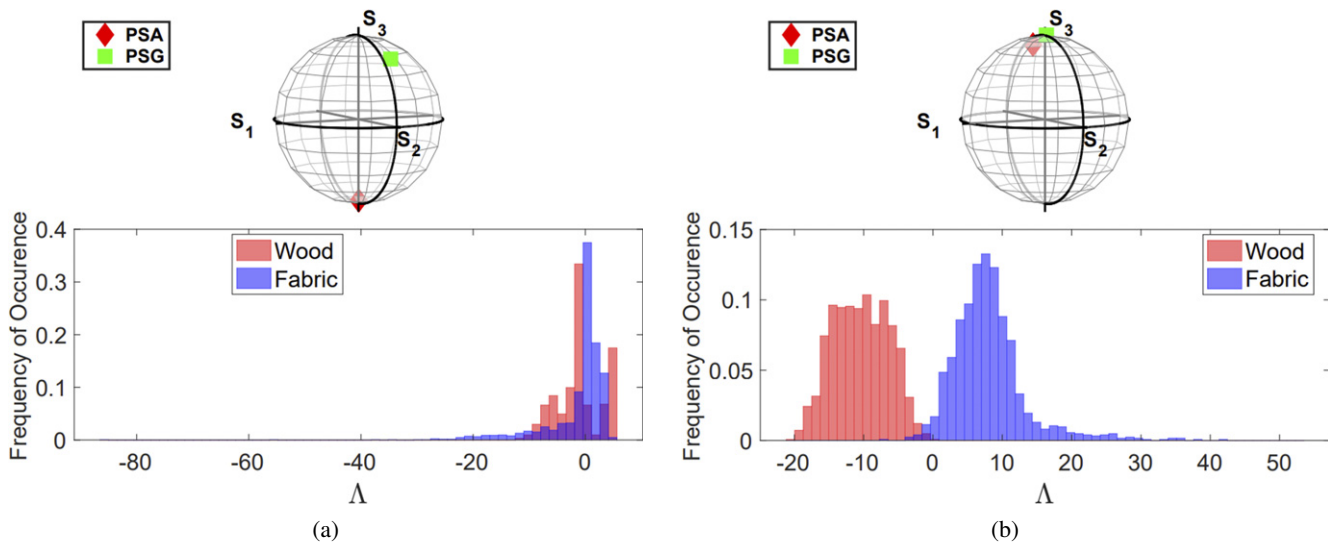= 0.78$ for $L = 1$ and $\overline{AUC} = 0.82$ for $L = 2$. For $L = 1$ the PSG is nearly right-circular polarized and PSA is nearly left-circular polarized. All PSG/PSA states are clustered around right-circular polarization for $L = 2$.

substitution results in a single Mueller matrix element $[\boldsymbol{M}]_{0,0}$ proportional to a measurement with an unpolarized PSA and an unpolarized PSG.

At three wavelengths and 12 scattering angles, these AUC estimates are reported in Table II. The ensemble of painted wood and fabric is selected so that the total reflectance (i.e., color) is similar and therefore the classification task using non-polarimetric imaging would be challenging. The AUC values in Table II are closest to 0.5 (i.e., guessing) at lower scattering angles and higher scattering angles. The AUC peaks at $\gamma = 80°$ for all three wavelengths. At this

acquisition geometry the mean is $\overline{AUC} = \{0.79, 0.70, 0.84\}$ for 451, 524, and 662 nm, respectively. To assess polarimetric measurements a single wavelength $\lambda = 524$ nm is selected since these AUC are lowest for the non-polarimetric imaging case.

Table III show AUC values for randomly selected PSG/PSA states using only $\lambda = 524$ nm measurements. AUC are tabulated over 12 scattering angles and 1–4 measurements. The $\overline{AUC}$ is close to 1.0 at a majority of scattering angles for three measurements or greater. This result indicates the potential to improve the material
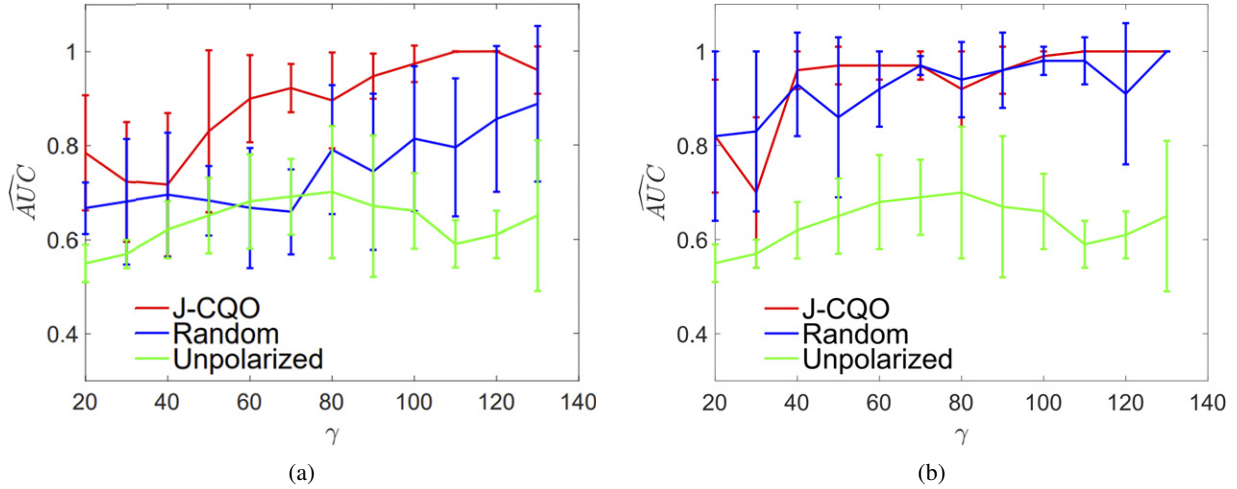
Figure 5. For (a) single measurement and (b) two measurements *AUC* estimates are compared for J-CQO (red), randomly selected PSG/PSA states (blue), and unpolarized (green) PSG/PSA states at $\lambda = 524$ nm. Mean and ± 1 standard deviation are reported as error bars. Classification improvement is seen between J-CQO and randomly selected PSG/PSA states at all scattering angles, γ, for a single measurement. For a single measurement, even randomly selected PSG/PSA states improve classification at most scattering angles as compared to imaging with unpolarized illumination and an unpolarized analyzer. This improvement over unpolarized PSG/PSA states increases for two measurements shown in (b). For two measurements the AUC difference between randomly selected PSG/PSA states and J-CQO decreases. The variance of the J-CQO AUC estimate is lower than randomly selected PSG/PSA states for a majority of scattering angles. As the number of polarimetric measurements increases the benefit of J-CQO optimization is expected to decrease.

Table IV. Estimates of *AUC* from **J-CQO optimized** PSG/PSA states. *AUC* is tabulated at varying scattering angles: γ and number of measurement: *L*. All results are for $\lambda = 524$ nm. The *AUC* at one measurement is greater than *AUC* from randomly selected PSG/PSA states reported in Table III. Similar to randomly selected PSG/PSA states *AUC* is close to 1.0 for two measurements or greater. Mean and standard deviation are reported from five perturbations of the testing and training sets.

γ/L	1	2	3	4
20°	0.78 ± 0.14	0.82 ± 0.12	0.87 ± 0.12	0.95 ± 0.14
30°	0.72 ± 0.14	0.76 ± 0.16	0.97 ± 0.02	0.96 ± 0.15
40°	0.72 ± 0.17	0.96 ± 0.04	0.99 ± 0.01	0.98 ± 0.02
50°	0.83 ± 0.19	0.97 ± 0.04	1.00 ± 0.00	1.00 ± 0.00
60°	0.90 ± 0.10	0.97 ± 0.03	1.00 ± 0.00	1.00 ± 0.00
70°	0.92 ± 0.06	0.97 ± 0.03	0.99 ± 0.01	1.00 ± 0.00
80°	0.89 ± 0.11	0.92 ± 0.08	1.00 ± 0.00	1.00 ± 0.00
90°	0.95 ± 0.05	0.96 ± 0.05	1.00 ± 0.00	1.00 ± 0.00
100°	0.97 ± 0.04	0.99 ± 0.01	1.00 ± 0.00	1.00 ± 0.00
110°	1.00 ± 0.00	1.00 ± 0.00	1.00 ± 0.00	1.00 ± 0.00
120°	1.00 ± 0.00	1.00 ± 0.00	1.00 ± 0.00	1.00 ± 0.00
130°	0.96 ± 0.06	1.00 ± 0.00	1.00 ± 0.00	1.00 ± 0.00

classification by optimizing the PSG/PSA states for one or two measurements.

Table IV are *AUC* values for J-CQO optimized PSG/PSA states using only $\lambda = 524$ nm measurements. For a single polarimetric measurement $\overline{AUC}$ is greater for J-CQO optimized than randomly selected PSG/PSA states at all scattering angles. For two measurements the mean *AUC* is also equal or greater for J-CQO optimized PSG/PSA except at $\gamma = \{30°, 80°\}$; here the mean values are close, within half of the standard deviation. At three and four measurements the

$\overline{AUC}$ differences between J-CQO optimized and randomly selected PSG/PSA states are within one standard deviation.

Cells from Tables III–IV are selected to report intermediate results: scattering angle $\gamma = 20°$ and number of measurements: $L = 1$, $L = 2$. In figures 3 and 4, the single measurement solution is shown in (a) and two measurements in (b). These PSG/PSA solutions are plotted on the Poincaré sphere and histograms of the test statistic Λ for randomly selected (Fig. 3) and J-CQO optimized (Fig. 4). The benefit of two measurements versus one is notable from the histograms of test statistics; this benefit is more pronounced for the J-CQO optimized solutions. At $L = 1$ the J-CQO optimized PSG is nearly right-circular polarized and PSA is nearly left-circular polarized. All PSG/PSA states are clustered around right-circular polarization for $L = 2$.

5. CONCLUSIONS

Polarized illumination and imaging effectively improve the discrimination accuracy of a diffuse, high albedo, metameric material data set. Improvements in discrimination accuracy are demonstrated when the generated and analyzed polarization states are both randomized or both optimized when compared to images using monochromatic unpolarized illumination and unpolarized imaging for scattering angles from 20° to 130°. Illumination wavelengths $\lambda = \{451, 524, 662\}$ nm are benchmarked for comparison; see Table II. Classification performance of $\overline{AUC} > 0.70$ is not achieved for $\lambda = 524$ nm using unpolarized monochromatic measurements at any scatter angle; see Figure 5. The highest value overall for unpolarized imaging is $\overline{AUC} = 0.84$ for 80° and $\lambda = 662$ nm. The wavelength of lowest classification performance for unpolarized imaging, $\lambda = 524$

nm, is selected to evaluated potential improvements from polarization imaging.

As compared to an unpolarized measurement, classification improved using a single randomly selected PSG/PSA state; see Fig. 5. The classification improvement is most pronounced at larger scattering angles where $\overline{AUC}$ increases $+0.20$; see Fig. 5. Using four polarimetric measurements at randomly selected PSG/PSA states yields a classification performance of $0.95 \leq \overline{AUC} \leq 1.0$ from scattering angles $20°\text{–}130°$.

Using J-CQO to select optimized PSG/PSA state achieves the same classification performance from a smaller number of measurements, as compared to randomly selected PSG/PSA states. The AUC values for one measurement from J-CQO optimized PSG/PSA states in Table IV are similar to the AUC values for two measurements from randomly selected PSG/PSA states in Table III. At three and four measurements the differences between J-CQO optimized and randomly selected PSG/PSA states are negligible. This result indicates that J-CQO optimization is capable of reducing the number of measurements without reducing classification performance.

This work demonstrates how J-CQO can be used to compute PSG/PSA pairs for which metameric materials in unpolarized color images become separable from a small number of monochromatic polarimetric measurements. Using these polarimetric measurements, materials can be classified without dependence on scene context. Analysis of optimal PSG/PSA states is intended for designing partial or adaptive Mueller imaging polarimeters.

REFERENCES

[1] R. Chipman, W. S. Tiffany, and G. Young, *Polarized Light and Optical Systems* (CRC Press, Boca Raton, FL, 2018).

[2] M. K. Kupinski, J. Bankhead, A. Stohn, and R. Chipman, "Binary classification of Mueller matrix images from an optimization of poincaré coordinates," J. Opt. Soc. Am. A **34**, 983–990 (2017).

[3] J. J. Gil and R. Ossikovski, *Polarized Light and the Mueller Matrix Approach* (CRC Press, Boca Raton, FL, 2016).

[4] R. M. A. Azzam, I. M. Elminyawi, and A. M. El-Saba, "General analysis and optimization of the four-detector photopolarimeter," J. Opt. Soc. Am. A **5**, 681–689 (1988).

[5] G. Anna, F. Goudail, P. Chavel, and D. Dolfi, "On the influence of noise statistics on polarimetric contrast optimization," Appl. Opt. **51**, 1178–1187 (2012).

[6] J. Scott Tyo, Z. Wang, S. J. Johnson, and B. G. Hoover, "Design and optimization of partial Mueller matrix polarimeters," Appl. Opt. **49**, 2326–2333 (2010).

[7] A. S. Alenin and J. S. Tyo, "Structured decomposition design of partial Mueller matrix polarimeters," J. Opt. Soc. Am. A **32**, 1302–1312 (2015).

[8] M. K. Kupinski, J. Rehbinder, H. Haddad, S. Deby, J. Vizet, B. Teig, A. Nazac, A. Pierangelo, F. Moreau, and T. Novikova, "Tasked-based quantification of measurement utility for ex vivo multi-spectral Mueller polarimetry of the uterine cervix," Proc. SPIE **10411**, 10411–10411-3 (2017).

[9] M. Kupinski, M. Boffety, F. Goudail, R. Ossikovski, A. Pierangelo, J. Rehbinder, J. Vizet, and T. Novikova, "Polarimetric measurement utility for pre-cancer detection from uterine cervix specimens," Biomed. Opt. Express **9**, 5691–5702 (2018).

[10] F. Le Roy-Brehonnet and B. Le Jeune, "Utilization of Mueller matrix formalism to obtain optical targets depolarization and polarization properties," Prog. Quantum Electron. **21**, 109–151 (1997).

[11] H. Chen and L. B. Wolff, "Polarization phase-based method for material classification in computer vision," Int. J. Comput. Vis. **28**, 73–83 (1998).

[12] S. R. Cloude and E. Pottier, "Concept of polarization entropy in optical scattering," Opt. Eng. **34**, 1599–1611 (1995).

[13] M. I. Mishchenko, *Electromagnetic Scattering by Particles and Particle Groups: An Introduction* (Cambridge University Press, New York, NY, 2014).

[14] NATO Advanced Research Workshop on Direct, Inverse Methods in Radar Polarimetry, and Wolfgang M. Boerner *Direct and Inverse Methods in Radar Polarimetry*, edited by W.-M. Boerner *et al* (Kluwer Academic Publishers: D. Reidel Dordrecht, Boston, 1992).

[15] S.-H. Baek, T. Zeltner, H. J. Ku, I. Hwang, X. Tong, W. Jakob, and M. H. Kim, "Image-based acquisition and modeling of polarimetric reflectance," ACM Trans. Graph. (Proc. SIGGRAPH 2020) **39** (2020).

[16] J. Zallat, P. Grabbling, and Y. Takakura, "Using polarimetric imaging for material classification," *Proc. 2003 International Conference on Image Processing (Cat. No. 03CH37429)* (IEEE, Piscataway, NJ, 2003), Vol. 2, p. II–827.

[17] I. J. Vaughn, B. G. Hoover, and J. S. Tyo, "Classification using active polarimetry," Proc. SPIE **8364**, 83640S (2012).

[18] Y. Quéau, F. Leporcq, A. Lechervy, and A. Alfalou, "Learning to classify materials using Mueller imaging polarimetry," Proc. SPIE **11172**, 11720Z (2019).

[19] N. Umow, "Chromatische depolarisation durch lichtzerstreuung," Phys. Z. **6**, 674–676 (1905).

[20] T. Germer, "Full four-dimensional and reciprocal mueller matrix bidirectional reflectance distribution function of sintered polytetrafluoroethylen," Appl. Opt. **56**, 9333–9340 (2017).

[21] J. M. López-Téllez, R. A. Chipman, L. W. Li, S. C. McEldowney, and M. H. Smith, "Broadband extended source imaging Mueller-matrix polarimeter," Opt. Lett. **44**, 1544–1547 (2019).

[22] F. Goudail and J. S. Tyo, "When is polarimetric imaging preferable to intensity imaging for target detection?," J. Opt. Soc. Am. A **28**, 46–53 (2011).

[23] M. K. Kupinski and E. Clarkson, "Method for optimizing channelized quadratic observers for binary classification of large-dimensional image datasets," J. Opt. Soc. Am. A **32**, 549–565 (2015).

[24] H. H. Barrett and K. J. Myers, *Foundations of Image Science* (John Wiley & Sons, Hoboken, NJ, 2013).

[25] C. E. Metz, "Receiver operating characteristic analysis: A tool for the quantitative evaluation of observer performance and imaging systems," J. Am. College Radiol. **3**, 413–422 (2006).

[26] W. T. G. Peterson, T. Birdsall, and W. Fox, "The theory of signal detectability," Trans. IRE Prof. Group Inf. Theory **4**, 171–212 (1954).

[27] W. S. Geisler, "Contributions of ideal observer theory to vision research," Vision Res. **51**, 771–781 (2011).